Seyedheydari, Fahime; Conley, Kevin M.; Thakore, Vaibhav; Karttunen, Mikko; Sihvola, Ari; Ala-Nissila, Tapio

Electromagnetic response of nanoparticles with a metallic core and a semiconductor shell

Published in:
Journal of Physics Communications

DOI:
10.1088/2399-6528/abd4c4

Published: 01/01/2021

Document Version
Publisher's PDF, also known as Version of record

Electromagnetic response of nanoparticles with a metallic core and a semiconductor shell

Journal of Physics Communications

OPEN ACCESS

RECEIVED
29 September 2020

REVISED
9 December 2020

ACCEPTED FOR PUBLICATION
17 December 2020

PUBLISHED
8 January 2021

PAPER

Electromagnetic response of nanoparticles with a metallic core and a semiconductor shell

Fahime Seyedheydari[1], Kevin M Conley[1,2], Vaibhav Thakore[3,4], Mikko Karttunen[3,4,5], Ari Sihvola[6] and Tapio Ala-Nissila[1,7]

[1] MSP Group, QTF Centre of Excellence, Department of Applied Physics, Aalto University School of Science, P O Box 11100, FI-00076 Aalto, Finland
[2] Department of Chemistry and Materials Science, Aalto University School of Chemical Engineering, P.O. Box 16100, FI-00076 Aalto, Finland
[3] Department of Applied Mathematics, The University of Western Ontario, London, Ontario N6A 5B7, Canada
[4] Center for Advanced Materials and Biomaterials Research, The University of Western Ontario, London, Ontario N6A 3K7, Canada
[5] Department of Chemistry, The University of Western Ontario, London, Ontario N6A 5B7, Canada
[6] Department of Electronics and Nanoengineering, Aalto University, P.O. Box 15500, FI-00076 Aalto, Finland
[7] Interdisciplinary Centre for Mathematical Modelling, Department of Mathematical Sciences, Loughborough University, Loughborough, Leicestershire LE11 3TU, United Kingdom

E-mail: tapio.ala-nissila@aalto.fi

Keywords: Core@Shell, plasmon, Lorenz-Mie theory, directional scattering

Abstract

We study the interplay between localized surface plasmon resonances from metallic cores and electromagnetic resonances from semiconducting shells in core@shell nanoparticles in the optical and near-infrared regions. To this end, we consider silver (Ag) spheres as plasmonically active nanoparticles with radii 20 nm, covered with shells of silicon (Si) up to 160 nm in thickness. We use the classical Lorenz-Mie theory to calculate the response of the core@shell nanoparticles to an external electromagnetic field that reveals a high degree of tunability of the Ag surface plasmons with a varying Si shell thickness, and a consequent merging of their Mie resonances. In contrast with pure metallic systems, the use of a low-bandgap semiconducting shell allows for a unique interrelation between its strong characteristic magnetic dipole mode and the localized surface plasmon resonance of the metallic core. This allows control over the forward and backward scattering efficiencies in the near-infrared in accordance with the predictions based on the Kerker conditions. Employing several other core@shell materials (Al@Si, Au@Si and Ag@Ge), we show that this approach to tailoring the absorption and scattering efficiencies, based on Kerker's conditions, can be further generalized to other similar core@shell systems.

1. Introduction

Metallic nanoparticles exhibit collective oscillations of their surface conduction electrons in an incident electromagnetic field. These localized surface plasmon resonances (LSPRs) have been extensively studied and employed in modern applications such as surface enhanced Raman scattering [1], optical fiber biosensors [2], sensing platforms [3], enhanced and superscattering [4], optical antennas [5], energy scavenging from the environment [6], and scattering cancellation and cloaking applications [7]. Plasmonic resonances emerge due to the high free carrier concentration in metallic systems, typically of the order of 10^{22} cm^{-3} [8]. The wavelength and intensity of the LSPRs depend on the material (conduction electron density), size, shape of the nanoparticles and the medium in which they are embedded [9]. In many cases, the dominant dipolar LSPR of metallic particles is in the near-ultraviolet or visible region due to the high plasma frequency, and metallic particles suffer from significant losses in the near-infrared (NIR) region [10]. To this end, doped conventional semiconductors such as silicon and germanium have been explored as potential candidates for plasmonics and nanophotonic applications in the NIR [11, 12]. Dopants change the electronic structure and influence the free charge carrier concentration by creating energy levels in the bandgap [13]. The minimum carrier concentration to obtain metal-like optical properties in the NIR for semiconductors, such as silicon, is about 10^{21} cm^{-3} [14].

Composite layers containing undoped low bandgap semiconductor microinclusions strongly reflect IR even at small volume fractions [15]. Calculations of the spectral response of layers containing bare and oxide-coated particles under irradiation from solar and blackbody emitters predict that the composites are useful as high temperature thermal radiation insulators or for improved absorption of NIR radiation in solar cells [16]. These properties would promote higher photovoltaic conversion efficiencies in ultra thin solar cells [6]. Further, reflectances of up to 90% at specific wavelengths could limit transmittance in sensing applications [17]. Conventional plasmonic metal particles in contact with an absorbing semiconductor, such as Si, have also been proposed to enhance broadband absorption in solar cells [18], and strong interaction has been observed between the Fano-type resonances of metal and excitons from semiconductor carbon nanotubes [19, 20]. It was also recently demonstrated that nanoparticles with a low bandgap semiconductor core covered by a metallic shell show the effects of plasmon hybridization [21]. The shape confinement of the metallic shell leads to the formation of interacting symmetric or anti-symmetric plasmon resonances [22–24]. The high permittivity of the semiconductor core enhances the magnitude of the anti-symmetric modes, allows high tunability of the resonance energies, and contributes additional modes [21].

While the plasmon hybridization offers ample possibilities to engineer the scattering and absorption spectrum of composite nanoparticles [25, 26], the degrees of freedom metal-oxide systems are limited to electric multipole modes. To this end, in this work we consider composite particles with a plasmonic core and a semiconductor shell. In such systems the plasmonic modes due to the metallic core are simpler than in the hybridized case. Importantly, however, the existence of the high-dielectric shell triggers both electric and magnetic resonance modes which, combined with the plasmonic resonances, opens up a rich parameter space to tune the absorption and scattering characteristics of the particles. Such small particles containing high permittivity materials can minimize losses and saturation in metamaterials with negative effective permittivity, permeability, and index of refraction [27–29]. Combining the exciton energy of semiconductor shell and the surface plasmon resonance excitation energy of metallic core then provides unique directional scattering properties and offers the exciting prospect of tailoring nanocomposite materials with stronger responses than can be obtained using bare metallic nanoparticles [30]. The interaction of arbitrarily shaped core@shell nanoparticles with light is well described using the full Maxwell equations [31, 32].

To study the interaction between plasmonic modes from a metallic core and modes from a semiconductor shell, we focus on spherical core@shell particles having a Ag core with a fixed 20 nm radius and covered by a Si shell with thickness up to 160 nm. First, the effective permittivity and dipolar resonances of the core@shell particles are qualitatively approximated using the quasistatic approach. Following this, we examine the absorption and scattering in the optical and NIR regions using full classical Lorenz-Mie (LM) theory. Our results reveal shifting and merging of the Ag LSPR and Si Mie resonances with increasing thickness of the shell. In particular, we demonstrate how the differential scattering can be tailored by adjusting the Si shell thickness due to the strong electric and magnetic resonances from Si. Additional modeling results for Ag@Ge, Al@Si and Au@Si are qualitatively similar and confirm the usefulness of metal@semiconductor nanoparticles for NIR applications.

2. Methods

The interaction of homogeneous and core@shell nanoparticles with light is accurately described by the classical LM theory in the visible and NIR region [33, 34]. The scattered field from a core@shell particle has an analytical solution, which is, in general, a superposition of the normal modes weighted by the corresponding Mie coefficients [34, 35]. In addition, the optical response of the core@shell particles is considered in the quasistatic approximation [33, 34, 36].

2.1. Metal@Semiconductor nanoparticles

In the present work, we consider primarily Ag@Si surrounded by a non-absorbing insulating medium with constant refractive index $n_{\mathrm{med}} = 1.5$ ($\varepsilon_{\mathrm{med}} = 2.25$) to represent a medium such as silica, oxide or polymer.

The materials within the particle are described by the frequency-dependent complex (relative) permittivity, ϵ. We show the real and imaginary parts of $\epsilon = \epsilon' + i\epsilon'' = (n_{\mathrm{r}} + ik)^2$ (where n_{r} is the refractive index and k is the absorption coefficient) for bulk Ag and Si in figures 2(A), (B). The permittivity data for Si and Ag are taken from Palik [37] and Johnson and Christy [38], respectively. Si is a low band gap semiconductor with a bandgap of 1.11 eV at $T = 300$ K [39].

The core@shell particles have a total radius R with the shell permittivity ε_2 and core radius r with permittivity ε_1 as shown schematically in figure 1. The Ag core radius is fixed at 20 nm, and the total particle radius R is increased up to 180 nm by adding a coating of Si on the Ag core. Quantum finite size effects are pronounced in particles with a radius much less than 20 nm [40], and the particles herein are thus sufficiently described using

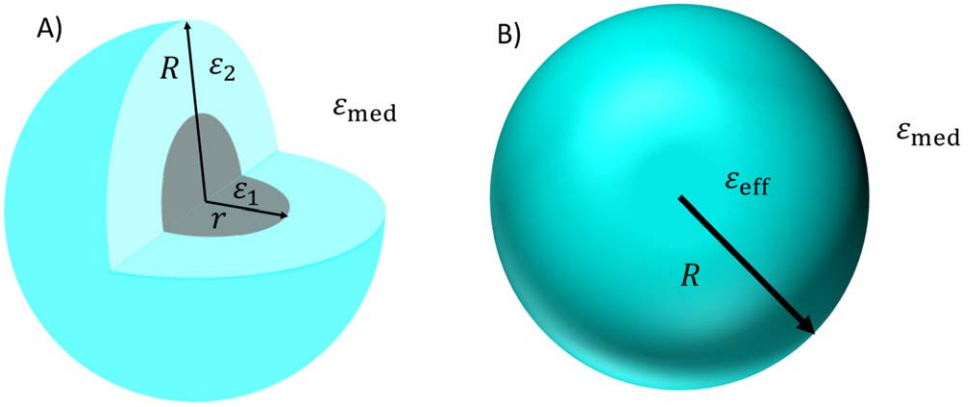

Figure 1. (A) Schematic of a spherical core@shell particle with total radius R and core radius r. The metal core, which has permittivity ε_1, is coated with a homogeneous semiconductor layer of uniform thickness $R - r$ and permittivity ε_2. (B) Schematic of an internally homogenized sphere with radius R and effective permittivity ε_{eff}. The permittivity of the host medium is $\varepsilon_{med} = 2.25$ in both cases.

the permittivity of bulk Ag and classical theory. Furthermore, metallic nanoparticles are commonly prepared using colloidal synthesis [41]. We also briefly discuss additional results for Ag@Ge, Al@Si and Au@Si nanoparticles in the last section.

2.2. Quasistatic approximation

It is useful to first consider the optical response in the quasistatic limit, where the particles become polarized in an external static field. Under the electrostatic approximation a sphere in an electrostatic field is equivalent to an ideal dipole.

When utilizing the quasistatic approximation, the core@shell particles will be 'internally homogenized' into a homogeneous spherical particle with effective permittivity, ε_{eff}, and total radius, R, as shown schematically in figure 1. The quasistatic polarizability of a core@shell particle is given by [34]

$$\alpha_1 = 4\pi\varepsilon_{med}\frac{R^3(\varepsilon_2 - \varepsilon_{med})(\varepsilon_1 + 2\varepsilon_2) + r^3(\varepsilon_1 - \varepsilon_2)(\varepsilon_{med} + 2\varepsilon_2)}{R^3(\varepsilon_2 + 2\varepsilon_{med})(\varepsilon_1 + 2\varepsilon_2) + 2r^3(\varepsilon_2 - \varepsilon_{med})(\varepsilon_1 - \varepsilon_2)}R^3, \tag{1}$$

while for a homogeneous sphere of permittivity ε_{eff} it simplifies to

$$\alpha_2 = 4\pi\varepsilon_{med}\frac{\varepsilon_{eff} - \varepsilon_{med}}{\varepsilon_{eff} + 2\varepsilon_{med}}R^3. \tag{2}$$

The effective permittivity of the internally homogenized core@shell particle can be obtained by combining equations (1) and (2) as [36]

$$\epsilon_{eff} = \epsilon_2\frac{R^3(\epsilon_1 + 2\epsilon_2) + 2r^3(\epsilon_1 - \epsilon_2)}{R^3(\epsilon_1 + 2\epsilon_2) - r^3(\epsilon_1 - \epsilon_2)}. \tag{3}$$

This equation for the effective permittivity will be used to qualitatively identify the energy of the dominant dipolar excitations in section 3.1.

The Fröhlich condition, which is valid for vanishingly small size parameter, arises by minimizing the denominator of equation (2) and where $\mathrm{Im}[\varepsilon_{eff}]$ is small.

$$\mathrm{Re}[\varepsilon_{eff}] = -2\varepsilon_{med}. \tag{4}$$

At $\varepsilon_{eff} \approx -2\varepsilon_{med}$ the polarizability becomes very large and is referred to as the dipolar surface plasmon resonance. The relation also explains the sensitivity of the plasmon resonance to its surroundings. The polarizability describes the characteristic resonances of a particle and the strength of its scattering efficiency.

In the electrostatic approximation the scattering efficiency of a small sphere is given by [34]

$$Q_{sca}^{static} = \frac{8}{3}y^4\left|\frac{\varepsilon_{eff} - \varepsilon_{med}}{\varepsilon_{eff} + 2\varepsilon_{med}}\right|^2, \tag{5}$$

where $y = 2\pi n_{med}R/\lambda$ is the size parameter. The backscattering efficiency for a small sphere is greater than the total scattering efficiency and is given by

$$Q_b^{static} = 4y^4\left|\frac{\varepsilon_{eff} - \varepsilon_{med}}{\varepsilon_{eff} + 2\varepsilon_{med}}\right|^2. \tag{6}$$

2.3. Lorenz-Mie theory for core@shell spheres

An analytical solution to Maxwell's equations yields the dielectric response of a spherical core@shell particle in an external electromagnetic field in terms of its characteristic electric and magnetic Mie coefficients a_n and b_n, respectively [33], as

$$a_n = \frac{\psi_n(y)[\psi_n'(m_2y) - A_n\chi_n'(m_2y)] - m_2\psi_n'(y)[\psi_n(m_2y) - A_n\chi_n(m_2y)]}{\xi_n(y)[\psi_n'(m_2y) - A_n\chi_n'(m_2y)] - m_2\xi_n'(y)[\psi_n(m_2y) - A_n\chi_n(m_2y)]}; \tag{7}$$

$$b_n = \frac{m_2\psi_n(y)[\psi_n'(m_2y) - B_n\chi_n'(m_2y)] - \psi_n'(y)[\psi_n(m_2y) - B_n\chi_n(m_2y)]}{m_2\xi_n(y)[\psi_n'(m_2y) - B_n\chi_n'(m_2y)] - \xi_n'(y)[\psi_n(m_2y) - B_n\chi_n(m_2y)]}, \tag{8}$$

where

$$A_n = \frac{m_2\psi_n(m_2x)\psi_n'(m_1x) - m_1\psi_n'(m_2x)\psi_n(m_1x)}{m_2\chi_n(m_2x)\psi_n'(m_1x) - m_1\chi_n'(m_2x)\psi_n(m_1x)}, \tag{9}$$

and

$$B_n = \frac{m_2\psi_n(m_1x)\psi_n'(m_2x) - m_1\psi_n(m_2x)\psi_n'(m_1x)}{m_2\chi_n'(m_2x)\psi_n(m_1x) - m_1\psi_n'(m_1x)\chi_n(m_2x)}, \tag{10}$$

where prime indicates differentiation with respect to the argument of the corresponding function, m_1 and m_2 are the refractive indices of the core and shell relative to the medium, and x is the size parameter of the core. The radial functions $\psi_n(x) = xj_n(x)$, $\xi_n(x) = \psi_n(x) + i\chi_n(x)$ and $\chi_n(x) = -xy_n(x)$ are Riccati-Bessel and Hankel functions where j_n, y_n are the spherical Bessel functions [34]. The order of the electric and magnetic modes are represented by N, where dipole corresponds to $N = 1$, quadrupole to $N = 2$, and so on.

The total scattering (Q_{sca}), absorption (Q_{abs}), back (Q_{b}) and forward scattering (Q_{f}) efficiencies [34] can be computed from

$$Q_{\text{sca}} = \frac{2}{y^2}\sum_{n=1}^{N}(2n+1)(|a_n|^2 + |b_n|^2), \tag{11}$$

$$Q_{\text{abs}} = \frac{2}{y^2}\sum_{n=1}^{N}(2n+1)[\text{Re}(a_n + b_n) - (|a_n|^2 + |b_n|^2)], \tag{12}$$

$$Q_{\text{b}} = \frac{1}{y^2}\left|\sum_{n=1}^{N}(2n+1)(-1)^n(a_n - b_n)\right|^2, \tag{13}$$

and

$$Q_{\text{f}} = \frac{1}{y^2}\left|\sum_{n=1}^{N}(2n+1)(a_n + b_n)\right|^2, \tag{14}$$

series are terminated after $y + 4y^{1/3} + 2$ terms In general, there is no simple relationship between the different scattering efficiencies, but if we assume that the dipolar modes with $N = 1$ dominate the response, we can easily see that $Q_{\text{sca}}^{N=1} = \frac{6}{y^2}(|a_1|^2 + |b_1|^2)$, $Q_{\text{b}}^{N=1} = \frac{9}{y^2}|(a_1 - b_1)|^2$ and $Q_{\text{f}}^{N=1} = \frac{9}{y^2}|(a_1 + b_1)|^2$. This implies that

$$\frac{Q_{\text{f}}^{N=1} + Q_{\text{b}}^{N=1}}{Q_{\text{sca}}^{N=1}} = 3. \tag{15}$$

We will show in the next section that this dipolar approximation gives a good qualitative understanding of the interplay between the different scattering efficiencies.

In the dipolar approximation one can also see that it is possible that the backward (forward) scattering vanishes, which happens for $a_1 - b_1 = 0$ ($a_1 + b_1 = 0$). This is called the first (second) Kerker condition and is a useful guide to tailor the differential scattering efficiencies using the Mie coefficients.

The sensitivity of the optical properties to variations in size was examined using ensembles of polydisperse nanoparticles with size distribution, $\rho(R)$. The particle size was normally distributed with average total radius, R_{avg}, and standard deviation, σ. The ensemble averaged backscattering efficiency is

$$Q_{\text{avg,b}} = \sum_i \rho(R_i)\, Q_{\text{b}}(R_i), \tag{16}$$

where i is the binning index [42], and similar expression for the ensemble averaged forward scattering efficiency.

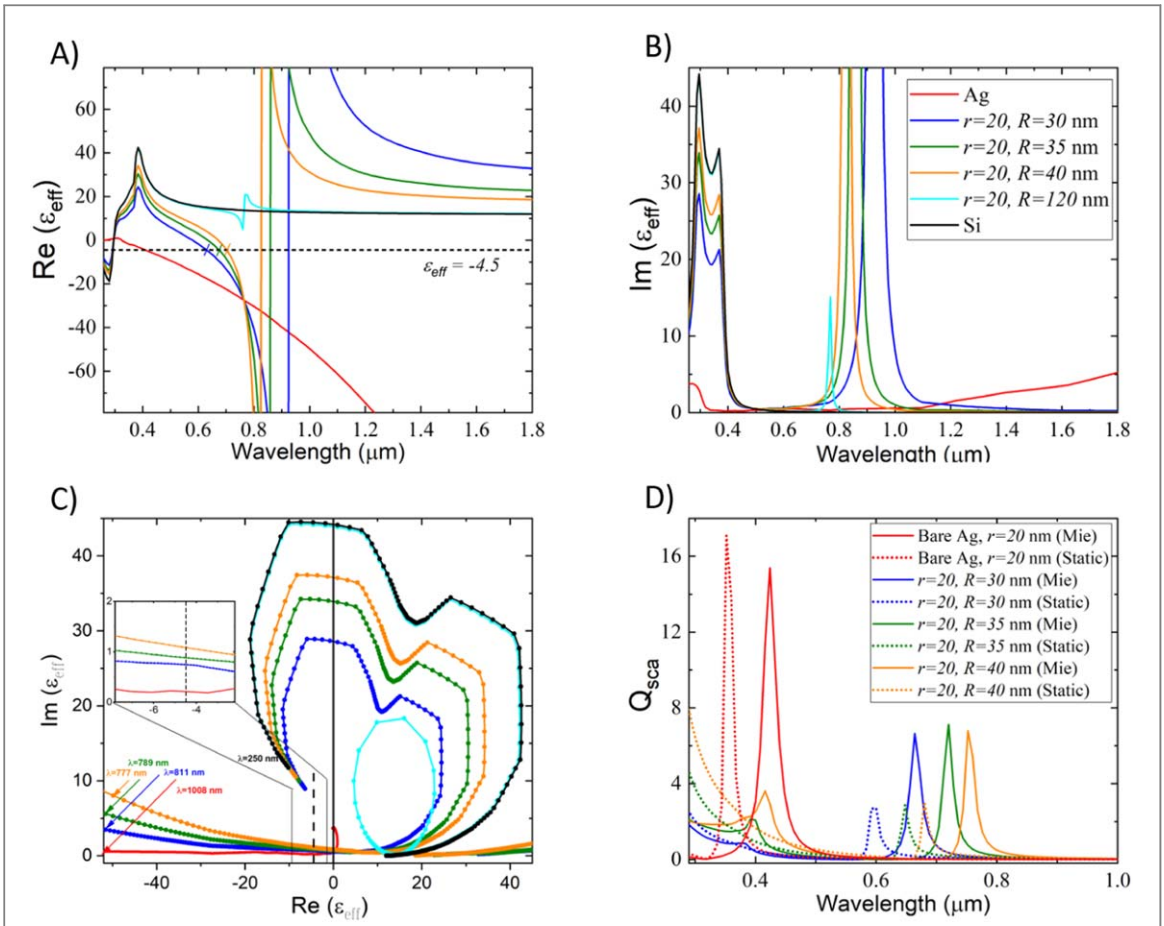

Figure 2. (A) The real part of the effective permittivity ε_{eff} from equation (3) for Ag nanoparticles ($r = 20$ nm) coated with Si and a varying total radius R. (B) The corresponding imaginary part of ε_{eff}. (C) Cole-Cole plots of ε_{eff}. The inset depicts the value of $\text{Im}[\varepsilon_{\text{eff}}]$ at the frequency where $\text{Re}[\varepsilon_{\text{eff}}]$ is -4.5, in the region $-8 < \text{Re}[\varepsilon_{\text{eff}}] < -2$. The dashed lines in (A) and (C) denote $\text{Re}[\varepsilon_{\text{eff}}] = -4.5$. (D) The scattering efficiency of a bare 20 nm Ag nanoparticle and different total radius R of Ag@Si nanoparticles calculated with the quasistatic approximation (dotted line) and the full Mie solution (solid line).

3. Results

3.1. Quasistatic approximation

In this subsection, we discuss the results from the quasistatic approximation of section 2.2 which allows the dominant dipolar resonances in a static external electric field to be identified. Plots of the real and imaginary part of the effective permittivities ε_{eff} for the Ag@Si (core@shell) nanoparticles are shown in figures 2(A)–(B). The core size is fixed at 20 nm and the total radius is 30, 35, 40 or 120 nm. A Cole-Cole plot [43], i.e. the imaginary *versus* the real part of the permittivities is presented in figure 2(C). First, the behavior of the effective permittivity is described and then it is used to calculate the scattering efficiencies of the effective, 'internally homogenized' particle (figure 2(D)).

At short wavelengths ($\lambda < 700$ nm), the effective permittivities of the core@shell particles are bracketed by the permittivity of the bulk core and shell materials. At longer wavelengths ($\lambda > 1$ μm), the effective permittivities of the core@shell particles approach the real part of the permittivity of bulk Si from larger values for increasing shell thickness. At intermediate wavelengths, there is a large fluctuation in the effective permittivities of the core@shell particles due to the strong dispersive effect and the function of equation (3). The heart-shaped regions ($\lambda = 250$ to $\lambda = 1800$ nm) of the Cole-Cole plots are a different feature which describes the interband transition region of Si (figure 2(C)).

The dipolar plasmon resonance occurs at $\text{Re}[\varepsilon_{\text{eff}}] \approx -2\varepsilon_{\text{med}} = -4.5$ for vanishingly small size parameter (equation (4)). This value is denoted by the dashed line in figures 2(A), (C). It can be seen that the addition of a high permittivity Si shell redshifts the plasmon. The plasmon shifts from about 632 nm to 704 nm when the shell thickness increases from 10 to 20 nm (figure 2(A)).

The imaginary component in the effective permittivity at the dipolar plasmon resonance condition accumulates with the increasing shell thickness as can be easily observed at the dashed line in the inset of figure 2(C). The strengthening indicates the surface plasmon will have more losses, and yet for particles with a

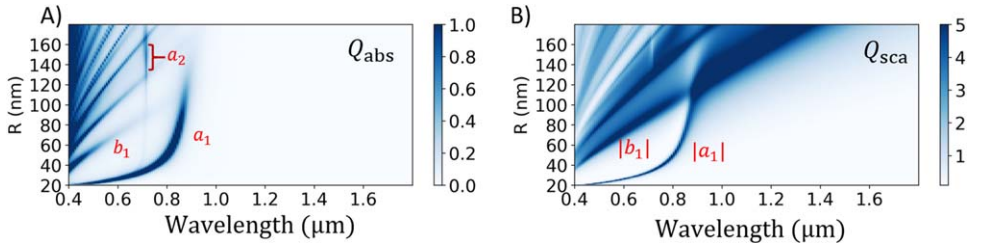

Figure 3. (A) The absorption efficiency, and (B) the total scattering efficiency as a function of the total radius R and wavelength λ for Ag@Si, where the core radius is fixed at $r = 20$ nm and the total radius varies from 20 to 180 nm. The particles are embedded in a medium with a refractive index of $n_{med} = 1.5$. Dominant Mie resonances are indicated by red letters in both panels.

thin shell, the intensity of the surface plasmon is likely maintained. In the particles with a thick shell, such as $R = 120$ nm, the effective permittivity approaches the permittivity of bulk Si and no longer reaches the resonance condition of -4.5 in this region. Thus the thick shell Ag@Si particles are no longer plasmonic.

The observations obtained from the resonance conditions are then validated by calculating the scattering efficiencies for the bare and the internally homogenized nanoparticles from the quasistatic approximation of equation (5). The scattering efficiencies of a bare Ag and core@shell Ag@Si with different total sizes ($R = 30$, 35, and 40 nm) are shown in figure 2(D). Similar to the redshift discussed in figure 2(A), the maximum of the scattering resonance redshifts with increasing total size. The scattering efficiency equation from the electrostatic approximation is valid for a small size parameter ($y \ll 1$), and here the size parameter of the particle with $R = 40$ nm, for example, is about 0.5 between $\lambda = 700$ to $\lambda = 800$ nm. Thus the electrostatic approximation cannot predict the position of resonances accurately compared with result from LM theory which are discussed in the next section.

3.2. Results from Lorenz-Mie Theory

3.2.1. Absorption and scattering efficiencies

In this section, we discuss results of the calculations from the full LM theory. The scattering efficiency obtained from LM theory are presented alongside the results from the quasistatic approximation in figure 2(D). The dipolar scattering mode predicted by the quasistatic approximation is consistently blueshifted from the full LM theory. The quasistatic approximation includes only the dipolar mode and overestimates its energy.

Next, the absorption and scattering efficiencies of the Ag@Si nanoparticles calculated from LM theory are discussed for core radius fixed at 20 nm and total radius up to 180 nm. The efficiencies display a rich multi-modal behavior in figures 3(A) and (B). The dominant low-energy Mie resonances are indicated on the plots. The maxima of the efficiencies shift to longer wavelengths as the dielectric shell is initially added. The unequal shifting of the dipolar electric and magnetic modes arises from the nature of the resonances. The dipolar electric mode is a plasmonic mode that is present in the bare Ag and Ag@Si particles with a thin shell discussed in the previous section. This plasmonic resonance shifts to longer wavelengths because m_2, the relative refractive index of the shell and medium, is greater than one. The effect of the change in the dielectric environment lessens as the shell becomes thicker, and consequently the shift of the plasmon resonance gradually diminishes. In contrast, the dipolar magnetic mode arises only once the semiconductor shell has been added and continues to shift unabated.

The origins of the resonances are validated by the Mie coefficients of a bare Ag particle ($r = 20$ nm) where the electric modes are far more pronounced than the magnetic modes. The contribution from the magnetic dipole mode greatly increases as the Si shell is added indicating that b_1 is a dielectric magnetic mode originating from the Si shell. While the metallic core is expected to have some influence on the dielectric modes originating in the shell, the core is small and there were no significant changes of the Mie coefficients of the bare Si particles in this range. With increasing shell thickness, the magnitude of the quadrupole electric mode (a_2) intensifies and is indicated in figure 3(A). The metallic core is responsible for this mode.

Due to the different nature of the resonances, the modes approach each other as the particle dimensions are adjusted. Initially the electric dipole mode associated with the Ag core redshifts rapidly up to about 0.75 μm with an increase in the Si shell thickness and then the rate of the redshift diminishes with further increase in the shell thickness. On the other hand, the magnetic Mie mode associated with the Si shell continues to redshift linearly with an increase in the shell thickness up to and beyond the point of degeneracy at $R = 100$ nm. For particles with a total radius of about 100 nm, the plasmonic electric and dielectric magnetic dipole modes are degenerate in energy and there occurs a strong overlap of the modes.

In particular, this degeneracy strengthens the scattering response of the core@shell particle in the NIR. For particles with the thickest dielectric shell, the higher order Mie coefficients also contribute to the scattering efficiency (figure 3(B)). By contrast, the magnitude of absorption efficiency decreases as the higher-order modes from the shell are excited (figure 3(A)).

It is possible that the outer Si shell partially oxidizes to silica in experiments. Silica has a smaller refractive index (approximately 1.45) than Si, and partial oxidation would reduce the effective relative refractive index of the shell to the medium, m_2. In addition, partial oxidation would decrease the thickness of the Si layer. Both decreasing the shell thickness and the dielectric environment of the core are expected to blueshift the Mie resonances and reduce their magnitude. The effect of oxidation has already been discussed in the case of semiconductor@oxide and metal@oxide particles in [9, 16]. Therefore, to avoid any undesirable diminished efficiency and shifting of the modes, oxidation of the Si shell should be kept minimal.

The synthesis of Au@Si nanoparticles embedded in silica matrix has reported using Au and SiO_2 atom beam co-sputtering and subsequent annealing [44]. It has been reported that by increasing the Si content in the shell, the LSPR peaks redshift and intensify. The experimental observations on small metal@semiconductor particles (diameter less than 4.6 nm) are in agreement with the computational results discussed herein. Further, computational methods can guide future experiments by calculating the properties of particles with a variety of dimensions. We also note that electrostatic calculations have been extremely successful at predicting the experimental optical properties of metal@oxide [3, 45, 46] and oxide@metal [22, 47] nanoparticles.

Another factor affecting the electromagnetic response in experiments comes from surface roughness that may lead to significant increase in scattering. The surface texture can be characterized using a roughness parameter which quantifies the size of the grooves relative to the incident wavelength. Previous computational studies have shown that the scattering by rough particles does not deviate strongly from smooth particles when the roughness parameter is less than 1, i.e., when the surface roughness is small compared with the wavelength [48]. Backscattering enhancement has been observed in laboratory-controlled optical experiments [49, 50], where a sharp peak of finite angular width is exhibited in backscattering from a random distribution of discrete scatterers. Cross-polarization scattering phenomena can also be involved in this process [51]. In near-earth astronomy, coherent backscatter from asteroids goes under the label opposition effect [52, 53]. Even if in these examples the scatterer sizes are considerably larger than the those in our study, we cannot neglect the possibility of the emergence of similar enhancement phenomena also in the nanoscale. This is an interesting topic that warrants further investigation.

3.2.2. Directional scattering and the Kerker condition

Due to the strong enhancement of the scattering of the Ag@Si particles in the NIR, it is of interest to understand the directional properties of the scattered field. Directional scattering can be useful for thermal NIR sensor applications to control heating or material degradation from radiation effects. The directional properties are conveniently analyzed using the Kerker conditions [54]; for more details see, e.g., [55–57]. As discussed in section 2.3, the backscattered radiation from a sphere is predicted to be zero when the electric (a_1) and magnetic (b_1) dipole coefficients coincide ($a_1 = b_1$) and other higher-order modes are negligible as per the first Kerker condition [58, 59].

This prediction is confirmed in the differential scattering efficiencies of Ag@Si with a core radius $r = 20$ nm that are presented in figure 4(A) for the backscattering and in figure 4(B) for the forward scattering directions. The backscattering efficiency vanishes for particle with a total radius of 120 nm coinciding with the degeneracy of the plasmonic electric and dielectric magnetic modes. The real and imaginary parts of the first two Mie coefficients a_1 and b_1 for particle with a total radius of 120 nm are shown in figure 4(C). The degeneracy is confirmed by an explicit inspection of the Mie coefficients. The dashed vertical lines in figures 4(C) and (D) at 944, 770, and 600 nm indicate where the contributions of the real parts from the dipolar electric and magnetic coefficients are equal. The most interesting case is that of wavelength $\lambda = 944$ nm, where the imaginary parts of a_1 and b_1 are also identical down to two decimal points, and thus the first Kerker condition ($a_1 - b_1 \approx 0$) is satisfied almost exactly. This indicates that interference between the scattered field from the plasmonic electric and dielectric magnetic modes is destructive in the backward direction. The total scattering is strong and forward scattering dominates. We note that due to the higher modes (included in figure 4(D)) the backscattering would never identically vanish even if the Kerker condition were precisely satisfied. This is most evident at $\lambda = 600$ nm, where the Kerker condition for dipolar modes is approximately true but the backscattering efficiency is actually very large.

It is also interesting to note that the forward scattering efficiency is significantly reduced between about 770 and 900 nm (figure 4(D)). In order to check the validity of the second Kerker condition, we have focused on the second indicated wavelength, at $\lambda = 770$ nm. As seen in figure 4(C) the real parts of a_1 and b_1 are equal while $\mathrm{Im}(a_1) = -\mathrm{Im}(b_1)$. This mismatch of phases is suggestive of the second Kerker condition of dipolar order ($a_1 + b_1 = 0$) but it requires the real component to be zero. Nevertheless, it is noteworthy that there is a broad

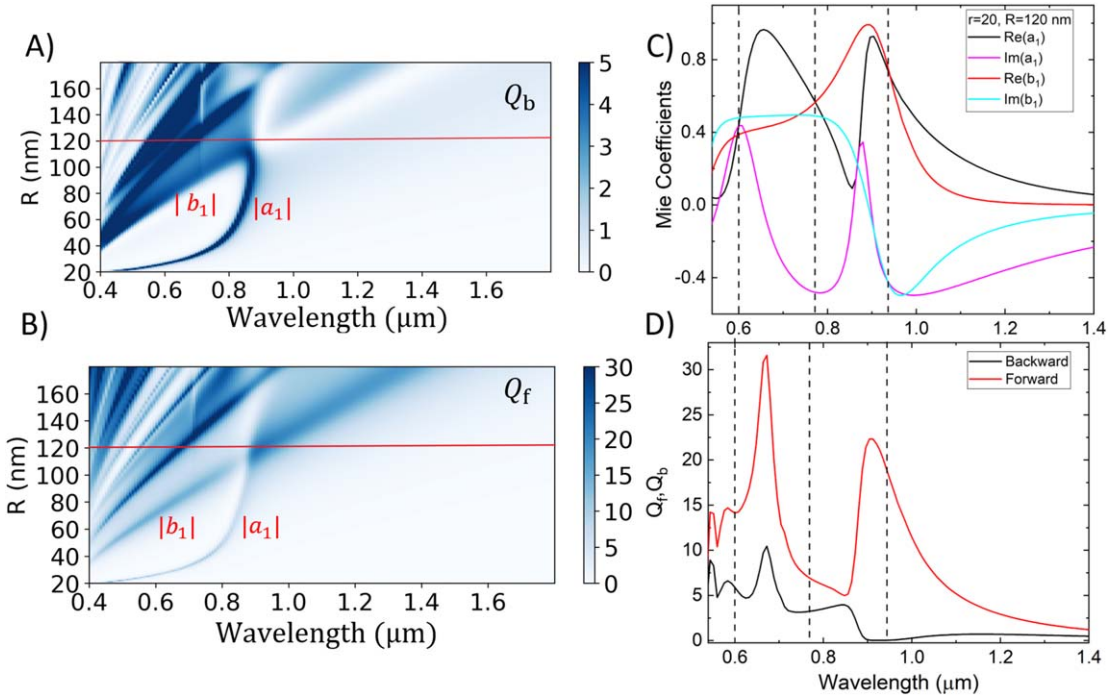

Figure 4. The differential scattering efficiencies for backscattering (A) and forward scattering (B) for Ag@Si with core radius fixed at 20 nm. (C) The dipolar electric (a_1) and magnetic (b_1) contributions to the scattering efficiency for the particle with a total radius of $R = 120$ nm (indicated in (A) and (B) by a red line). (D) The forward (red line) and backward (black line) scattering efficiencies for the particle with a total radius of $R = 120$ nm.

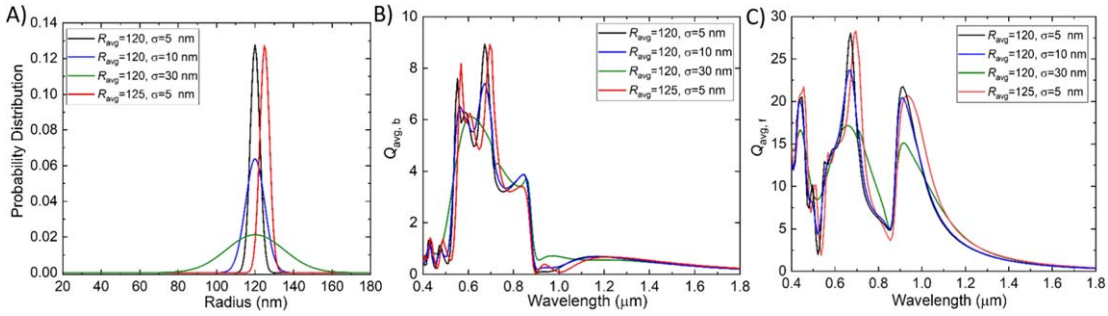

Figure 5. (A) The size distributions of Ag@Si particles with normal distributions with average total particle radius of either $R_{avg} = 120$ or 125 nm and standard deviations $\sigma = 5$, 10, or 30 nm. (B) The backward and (C) forward scattering efficiencies of an ensemble of particles with the size distribution in (A).

spectral range in which the modes are out of phase and a considerable decrease in the forward scattering efficiency is observed. The zero backscattering efficiency for a given particle dimension can be easily explained by identifying the exact mode composition. This comes from the overlap of the dielectric magnetic mode (b_1) and the electric mode (a_1) which satisfies the first Kerker condition. For practical applications, the wavelength of the forward-directed scattering with zero backscattering can be manipulated by changing the materials.

To check the optical properties under realistic experimental conditions, we examined how the scattering efficiency of the particle satisfying the Kerker condition, i.e., with average total radius of 120 nm, would change if it were part of an ensemble of polydisperse Ag@Si nanoparticles. To this end, the backward and forward scattering efficiencies of an ensemble of particles with a normally distributed total radius, R_{avg}, of 120 nm and standard deviations $\sigma = 5$, 10, or 30 nm were calculated. The backward and forward scattering efficiencies, $Q_{avg,b}$ and $Q_{avg,f}$, in figures 5(B)–(C) show that the backscattering efficiency remains zero in polydisperse samples with σ less than 10 nm. The backscattering efficiency increases and the peaks broaden as the size distribution of the particle ensemble broadens due to the increased contribution from particles which do not satisfy the Kerker condition. We note that 95.5% of the particles are between 100 and 140 nm in the distribution with $R_{avg} = 120$ nm and standard deviation of 10 nm. A particle with a radius of 140 nm is 17% larger by radius

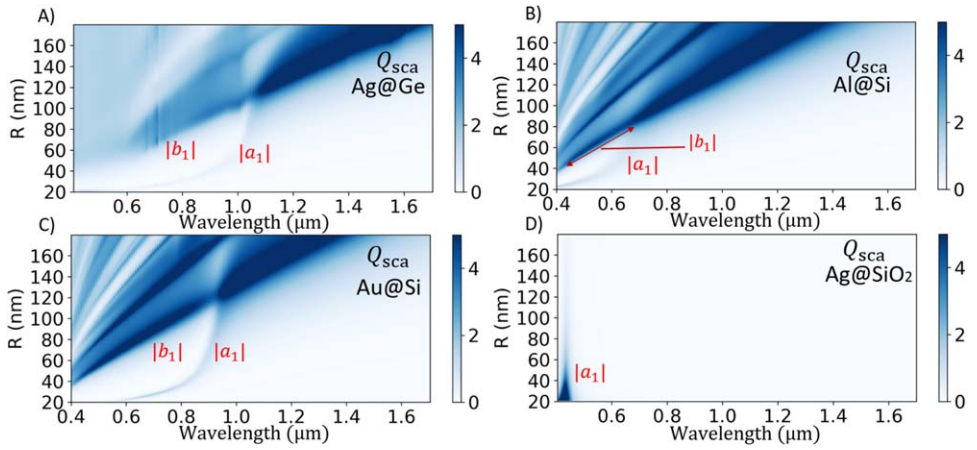

Figure 6. The total scattering efficiency as a function of the total radius R and wavelength λ. Here the core radius is fixed at $r = 20$ nm and the total radius varies from 20 to 180 nm for (A) Ag@Ge, (B) Al@Si, (C) Au@Si, and (D) Ag@SiO_2 nanoparticles. The particles are embedded in a host medium with a refractive index of $n_{med} = 1.5$.

than the mean size. Thus, the zero backscattering spectral region is very resistant to variations in the total size. We also examined polydisperse Ag@Si particles with a different average total radius ($R_{avg} = 125$ nm). Interestingly, in the case of $R_{avg} = 125$ nm and $\sigma = 5$ nm the backscattering efficiency (figure 5B) has two minima between wavelengths 850 and 1050 nm.

Increasing the core radius will also redshift the wavelength of the zero backscattering as the intersection of the electric and magnetic modes occur for a thicker Si shell. For example, the wavelength of the zero backscattering efficiency at $\lambda = 944$ nm for the $r = 20$ nm particle shifts to $\lambda = 1042$ nm for $r = 30$ nm. The total size of the particle also needs to be larger, namely 135 nm instead of 120 nm.

3.2.3. Core@Shell particles containing other materials

Finally, we examine the effects of (a) changing the shell material to another low bandgap semiconductor, Ge, which has a bandgap of 0.66 eV, and, (b) the core material alternatively to Al (dipolar LSPR at 82.6 nm) or Au (dipolar LSPR at 500 nm). Ge and Si are both indirect band gap semiconductors but differ significantly in the values of their dielectric permittivity and bandgap.

In figure 6, we show the total scattering efficiencies for Ag@Ge, Al@Si and Au@Si nanoparticles with the core fixed at $r = 20$ nm. The scattering efficiencies of Ag@Ge shift to longer wavelengths than the Ag@Si nanoparticles (figure 3(B)) due to an increase in the permittivity of the shell at these wavelengths. Furthermore, this strong redshift is accompanied by large losses that weaken Q_{sca}. Similar to the Ag@Si, the Ag@Ge particle has a magnetic dipole mode that interferes with the electric mode to satisfy the first Kerker condition for characteristic particle dimensions. However, the magnetic dielectric and plasmonic electric dipole modes for Ag@Ge are degenerate at $\lambda = 1080$ nm for a particle with a total radius about 100 nm (figure 6(A)). In contrast, these modes are degenerate at $\lambda = 890$ nm for the Ag@Si particles (figure 3(B)).

The robustness of this approach to tailoring the forward and backscattering response of the nanoparticles for different wavelength regions is further confirmed when the core material is changed to either Al or Au. The a_1 mode in the particle with a Ag, Al, or Au core have similar redshifts upon coating with a high permittivity semiconductor shell. This redshift is due to the value of the relative refractive index of the shell to that of the host, m_2, is greater than one. Yet the a_1 mode in each of the bare Al, Au, and Ag nanoparticles are at distinct energies, and so the redshift originates at different wavelength. In particular, comparing the scattering efficiencies of Ag@Si in figure 3(B) with those of Al@Si and Au@Si in figures 6(B) and (C) shows the similarity of their behavior. In all cases, an overlap of the Mie resonances associated with the core and the shell strongly enhances scattering. The magnetic and electric dipolar resonances merge at $\lambda = 1080$ nm, $\lambda = 680$ nm and $\lambda = 940$ nm for Ag@Ge, Al@Si and Au@Si particles with a total radius of 115 nm, 85 nm and 120 nm, respectively. The particles with a Ag or Au core merge in the NIR, but the merger for the Al core occurs in the visible region. Figure 6(D) shows the scattering efficiency of the metallic core covered with dielectric shell (Ag@SiO_2). The stark difference between the oxide and the semiconductor coating clearly illustrates the importance of semiconductor shells and their magnetic mode which is required to satisfy the Kerker condition in these configurations.

4. Conclusions

The core@shell particles here display a rich variety of electric and magnetic Mie resonances that produce significant changes in the absorption and scattering properties. We have proposed a design with metal@semiconductor nanocomposites that is of great interest due to their size-dependent optical and electronic properties. We have focused on the effects of particle dimensions and material on the backward and forward scattering in the visible and near-IR regions, and described the origin of the phenomena observed using fundamental physical concepts (the Kerker conditions). To this end, we have studied the optical properties of metal@semiconductor (Ag@Si, Ag@Ge, Al@Si and Au@Si) spherical nanoparticles of total radii 20–180 nm with a focus on the influence of a layer of Si on a Ag core in the visible and near-IR regions using the quasistatic approximation and the full Lorenz-Mie theory. The presence of a plasmon resonance for thin shell was confirmed in the quasi-static approximation using an effective permittivity for this core@shell configuration.

The use of Ag nanoparticles as a core with an optimized dimension in this arrangement yields increased absorption efficiency in the visible and infrared (IR) range while the absorption efficiency peaks of a bare Si of the same dimension are observed at wavelengths in the ultraviolet (UV) range. The LSPRs associated with the Ag core redshift and are modulated as the encapsulating dielectric environment changes from the non-absorbing host medium to the increasing thickness of the high-permittivity semiconducting Si shell. Although the resonances might be thought of as arising from either the core (such as the plasmonic dipolar electric mode) or the shell (such as the dielectric dipolar magnetic mode), this simplistic description does not quite illustrate the intricate interplay between the resonances that occur within the core@shell particle. Our results show that the scattering modes characteristic of a core@shell particle are a complex amalgamation of the particle dimensions, core and shell materials, and its environment.

The Ag@Si particles with a 20 nm core and a total radius 120 nm exhibit degenerate dipolar electric and magnetic Mie resonances with zero backscattering efficiency at $\lambda = 944$ nm as a result of satisfying the first Kerker condition. Similar minimization of the backscattering is also observed for Ag@Ge, Al@Si and Au@Si nanoparticles. Particles with a core radius of 20 nm and a total radii of 120, 75 and 100 nm satisfy this condition for Au@Si, Al@Si and Ag@Ge particles at $\lambda = 950$, $\lambda = 650$ and $\lambda = 1030$ nm, respectively. Due to the different characteristic positions of the LSPRs, the first Kerker condition is satisfied at a different wavelength and dimensions for these particles. Furthermore, the Ag@Si particles have a broad spectral range between 770 and 900 nm where in there occurs minimal forward scattering.

The analysis of the complex electromagnetic interaction triggered by the electric plasmonic modes of the silver core and the magnetic modes created in the high-dielectric layer makes our work particularly interesting for applications. It gives both physical intuition into the manner these modes affect each other's spectral shifts and recipes how to engineer core–shell objects with optimally responding structure, in particular towards enhanced or minimized reflection efficiency. The results should thus be useful for experimental and theoretical design of plasmonically enhanced applications in the near-IR [60, 61].

Despite employing a simple spherical geometry for the core@shell particles, quite a lot of interesting physics follows nevertheless. Thus, a natural extension would be to 'squeeze' the sphere and consider an ellipsoidal shape since the quasi-static analysis (although not full Lorenz- Mie) can be extended to those geometries, and the qualitative behavior estimated there from. Further shape modification could be towards quasicubes, superspheres [62] but since one cannot find analytical solutions in the quasistatic case for these, it would require to resorting to numerical methods such as the surface-integral-equation methods [63].

Acknowledgments

We wish to thank Pasi Ylä-Oijala for useful discussions. This work was performed as part of the Academy of Finland project 314 488 and QTF Centre of Excellence program (project 312 298) (FS, KC, TAN). MK was supported by the Natural Sciences and Engineering Research Council of Canada (NSERC) and the Canada Research Chairs Program. We acknowledge computational resources provided by CSC—IT Center for Science (Finland) and by the Aalto Science-IT project (Aalto University School of Science).

The data that supports the findings of this study are available within the article and upon request.

ORCID iDs

Fahime Seyedheydari https://orcid.org/0000-0002-0402-2202
Kevin M Conley https://orcid.org/0000-0001-7780-3096
Vaibhav Thakore https://orcid.org/0000-0001-9368-7945

Mikko Karttunen https://orcid.org/0000-0002-8626-3033
Ari Sihvola https://orcid.org/0000-0001-7661-8913
Tapio Ala-Nissila https://orcid.org/0000-0002-3210-3181

References

[1] Lu L, Kobayashi A, Tawa K and Ozaki Y 2006 *Chem. Mater.* **18** 4894–901
[2] Chen J, Shi S, Su R, Qi W, Huang R, Wang M, Wang L and He Z 2015 *Sensors* **15** 12205–17
[3] Aslan K, Wu M, Lakowicz J R and Geddes C D 2007 *J. Am. Chem. Soc.* **129** 1524–5
[4] Ruan Z and Fan S 2010 *Phys. Rev. Lett.* **105** 013901
[5] Agio M and Alù A (ed) 2013 *Optical Antennas* (Cambridge, UK: Cambridge University Press) (https://doi.org/10.1017/CBO9781139013475)
[6] Atwater H A and Polman A 2010 *Nat. Mater.* **9** 205
[7] Chen P Y, Soric J and Alu A 2012 *Adv. Mater.* **24** OP281–OP304
[8] Agrawal A, Cho S H, Zandi O, Ghosh S, Johns R W and Milliron D J 2018 *Chem. Rev.* **118** 3121–207
[9] Laaksonen K, Suomela S, Puisto S R, Rostedt N K, Ala-Nissila T and Nieminen R M 2013 *J. Opt. Soc. Am.* B **30** 338–48
[10] West P R, Ishii S, Naik G V, Emani N K, Shalaev V M and Boltasseva A 2010 *Laser Photonics Rev.* **4** 795–808
[11] Naik G V and Boltasseva A 2010 *Phys. Status Solidi* **4** 295–7
[12] Paniagua-Domínguez R, López-Tejeira F, Marqués R and Sánchez-Gil J A 2011 *New J. Phys.* **13** 123017
[13] Mendelsberg R J, Garcia G, Li H, Manna L and Milliron D J 2012 *J. Phys. Chem.* C **116** 12226–31
[14] Naik G V, Shalaev V M and Boltasseva A 2013 *Adv. Mater.* **25** 3264–94
[15] Tang J, Thakore V and Ala-Nissila T 2017 *Sci. Rep.* **7** 5696
[16] Conley K M, Thakore V, Seyedheydari F, Karttunen M and Ala-Nissila T 2020 *AIP Adv.* **10** 095128
[17] Conley K, Thakore V and Ala-Nissila T 2018 Plasmonically enhanced spectrally-sensitive coatings for gradient heat flux sensors *2018 Progress in Electromagnetics Research Symposium (PIERS-Toyama) (Toyama, Japan, 1-4 Aug. 2018)* (IEEE) pp 2435–41 978-4-8855-2316-8
[18] Pala R A, White J, Barnard E, Liu J and Brongersma M L 2009 *Adv. Mater.* **21** 3504–9
[19] Nikolaenko A E, De Angelis F, Boden S A, Papasimakis N, Ashburn P, Di Fabrizio E and Zheludev N I 2010 *Phys. Rev. Lett.* **104** 153902
[20] Luk'yanchuk B, Zheludev N I, Maier S A, Halas N J, Nordlander P, Giessen H and Chong C T 2010 *Nat. Mater.* **9** 707–15
[21] Seyedheydari F, Conley K and Ala-Nissila T 2020 *Photonics* **7** 10
[22] Prodan E, Radloff C, Halas N J and Nordlander P 2003 *Science* **302** 419–22
[23] Laaksonen K, Suomela S, Puisto S, Rostedt N, Ala-Nissila T and Nieminen R 2014 *J. Opt. Soc. Am.* B **31** 494–502
[24] Sihvola A, Tzarouchis D C, Ylä-Oijala P and Wallén H 2018 Properties of hybridized modes in core-shell scatterers *2018 II URSI Atlantic Radio Science Meeting (AT-RASC) (Meloneras, Spain, 28 May-1 June 2018)* (IEEE) pp 1–3 978-90-82598-73-5
[25] Yildiz B, Habib M, Rashed A and Caglayan H 2019 *J. Appl. Phys.* **126** 113104
[26] Tzarouchis D C and Sihvola A 2018 *Phys. Rev. Appl.* **10** 054012
[27] Veselago V G 1967 *Usp. Fiz. Nauk* **92** 517
[28] Wheeler M S, Aitchison J S and Mojahedi M 2006 *Phys. Rev.* B **73** 045105
[29] Jylhä L, Kolmakov I, Maslovski S and Tretyakov S 2006 *J. Appl. Phys.* **99** 043102
[30] Nieto-Vesperinas M, Gomez-Medina R and Saenz J 2011 *J. Opt. Soc. Am.* A **28** 54–60
[31] Ammari H, Ruiz M, Yu S and Zhang H 2016 *J. Differ. Equ.* **261** 3615–69
[32] Ammari H, Fitzpatrick B, Hiltunen E O, Lee H and Yu S 2019 *J. Differ. Equ.* **267** 4719–44
[33] Aden A L and Kerker M 1951 *J. Appl. Phys.* **22** 1242–6
[34] Bohren C F and Huffman D R 1983 A Potpourri of Particles *Absorption and scattering of light by small particles* (Weinheim, Germany: Wiley) pp 181–3
[35] Kreibig U 1974 *J. Phys. F: Met. Phys.* **4** 999
[36] Chettiar U K and Engheta N 2012 *Opt. Express* **20** 22976–86
[37] Palik E D 1998 *Handbook of optical constants of solids* (Vol. 3) (San Diego, CA: Academic Press) 5–114
[38] Johnson P B and Christy R W 1972 *Phys. Rev.* B **6** 4370
[39] Streetman B G and Banerjee S 2001 *Solid State Electronic Devices* (New Delhi, India: Prentice-Hall of India) 524
[40] Shabaninezhad M and Ramakrishna G 2019 Theoretical Investigation of Plasmonic Properties of Quantum-Sized Silver Nanoparticles *Plasmonics* **15** 783–795
[41] Jia C J and Schüth F 2011 *Phys. Chem. Chem. Phys.* **13** 2457–87
[42] Merikallio S 2016 Computer modeling of light scattering by atmospheric dust particles with spheroids and ellipsoids *Ph.D Thesis* Aalto University
[43] Cole K S and Cole R H 1941 *J. Chem. Phys.* **9** 341–51
[44] Mohapatra S, Mishra Y, Avasthi D, Kabiraj D, Ghatak J and Varma S 2008 *Appl. Phys. Lett.* **92** 103105
[45] Kobayashi Y, Katakami H, Mine E, Nagao D, Konno M and Liz-Marzán L M 2005 *J. Colloid Interface Sci.* **283** 392–6
[46] Shanthil M, Thomas R, Swathi R and George Thomas K 2012 *J. Phys. Chem. Lett.* **3** 1459–64
[47] Loo C, Lin A, Hirsch L, Lee M H, Barton J, Halas N, West J and Drezek R 2004 *Technol. Cancer Res. Treat.* **3** 33–40
[48] Li C, Kattawar G W and Yang P 2004 *J. Quant. Spectrosc. Radiat. Transf.* **89** 123–31
[49] Kuga Y and Ishimaru A 1984 *J. Opt. Soc. Am.* A **1** 831–5
[50] Tsang L and Ishimaru A 1984 *J. Opt. Soc. Am.* A **1** 836–9
[51] Jordan D and Moreno F 1993 *J. Opt. Soc. Am.* A **10** 1989–95
[52] Lindqvist H, Muinonen K and Nousiainen T 2009 *J. Quant. Spectrosc. Radiat. Transf.* **110** 1398–410
[53] Mishchenko M I 2009 *J. Quant. Spectrosc. Radiat. Transf.* **110** 1210–22
[54] Kerker M, Wang D S and Giles C 1983 *J. Opt. Soc. Am.* A **73** 765–7
[55] Zambrana-Puyalto X, Fernandez-Corbaton I, Juan M L, Vidal X and Molina-Terriza G 2013 *Opt. Lett.* **38** 1857
[56] Shibanuma T, Albella P and Maier S A 2016 *Nanoscale* **8** 14184–92
[57] Luk'yanchuk B, Paniagua-Domínguez R, Kuznetsov A I, Miroshnichenko A E and Kivshar Y S 2017 *Phil. Transact. Roy. Soc.* A **375** 20160069
[58] Liu W, Zhang J, Lei B, Ma H, Xie W and Hu H 2014 *Opt. Express* **22** 16178–87

[59] García-Cámara B, Gómez-Medina R, Sáenz J J and Sepúlveda B 2013 *Opt. Express* **21** 23007–20
[60] Slovick B A, Baker J M, Flom Z and Krishnamurthy S 2015 *Appl. Phys. Lett.* **107** 141903
[61] Conley K, Moosakhani S, Thakore V, Ge Y, Lehtonen J, Karttunen M, Hannula S P and Ala-Nissila T 2020 Silica-silicon composites for near-infrared reflection: A comprehensive computational and experimental study (arXiv:2009.13805 [physics.app-ph])
[62] Tzarouchis D, Ylä-Oijala P and Sihvola A 2019 *Photonics* **6** 18
[63] Ylä-Oijala P, Taskinen M and Järvenpää S 2005 Surface integral equation formulations for solving electromagnetic scattering problems with iterative methods *Radio Sci.* **40** 1–19